Chemistry & Biology
Article

High-Density Targeting of a Viral Multifunctional Nanoplatform to a Pathogenic, Biofilm-Forming Bacterium

Peter A. Suci,[1,2,3] Deborah L. Berglund,[3] Lars Liepold,[2,4] Susan Brumfield,[5] Betsey Pitts,[3] Willy Davison,[3,6] Luke Oltrogge,[2,4] Kathryn O. Hoyt,[3] Sarah Codd,[7] Philip S. Stewart,[3,6] Mark Young,[1,2,5,*] and Trevor Douglas[2,4,*]
[1] Department of Microbiology
[2] Center for BioInspired Nanomaterials
[3] Center for Biofilm Engineering
[4] Department of Chemistry and Biochemistry
[5] Department of Plant Sciences
[6] Department of Chemical and Biological Engineering
[7] Department of Mechanical and Industrial Engineering
Montana State University, Bozeman, MT 59717, USA
*Correspondence: myoung@montana.edu (M.Y.), tdouglas@chemistry.montana.edu (T.D.)
DOI 10.1016/j.chembiol.2007.02.006

SUMMARY

Nanomedicine directed at diagnosis and treatment of infections can benefit from innovations that have substantially increased the variety of available multifunctional nanoplatforms. Here, we targeted a spherical, icosahedral viral nanoplatform to a pathogenic, biofilm-forming bacterium, *Staphylococcus aureus*. Density of binding mediated through specific protein-ligand interactions exceeded the density expected for a planar, hexagonally close-packed array. A multifunctionalized viral protein cage was used to load imaging agents (fluorophore and MRI contrast agent) onto cells. The fluorescence-imaging capability allowed for direct observation of penetration of the nanoplatform into an *S. aureus* biofilm. These results demonstrate that multifunctional nanoplatforms based on protein cage architectures have significant potential as tools for both diagnosis and targeted treatment of recalcitrant bacterial infections.

INTRODUCTION

Although conventional antimicrobial therapies effectively resolve most infections, exceptions to this probable outcome constitute a significant health concern [1, 2]. Each new antibiotic introduced to control emergent resistant strains of microbes has a limited lifespan [3–7], and communities of microbes that colonize both biomaterial and tissue surfaces typically possess an intrinsic transient resistance to a broad spectrum of antimicrobial agents [1, 8–11]. Biofilm infections are not only recalcitrant to treatment, but they are also difficult to diagnose since the infective communities spend substantial periods of time in relative quiescence, producing classic symptoms of infection only sporadically [1]. One of the most prominent bacterial players in multidrug resistance, *S. aureus*, is also a common biofilm-forming pathogen [12–16]. Thus, for certain categories of *S. aureus* infections, iatrogenically acquired drug resistance and transient intrinsic resistance of biofilms must be confronted en masse.

The realization that conventional antimicrobial therapies and diagnostic techniques will always be limited in their ability to cope with certain types of infections has fostered a resurgence of interest in previously explored alternatives such as bacteriophage therapy [17, 18] and photodynamic therapy [19, 20]. Substantial effort has been directed at developing liposome and dendrimer platforms for targeted delivery of antimicrobial agents to microbial pathogens [21–27]. A variety of novel systems based on both synthetic [28–31] and biological [32] materials has been explored for diagnosis and treatment of tumors. This expansive repertoire is beginning to be tapped to develop and implement new approaches to infection control [33].

We have been developing a family of multifunctional nanoplatforms for biomedical applications that are based on self-assembling, supramolecular, symmetrical protein architectures [34–36]. The protein cage library includes viral capsids [37–40], ferritins [41–45], heat-shock proteins [34, 46, 47], and putative DNA-binding proteins [48, 49]. One of the best-characterized protein cages is cowpea chlorotic mottle virus (CCMV), a 28 nm icosahedral plant virus that can be produced as a noninfectious protein cage architecture [50, 51]. The structure of CCMV is known at the atomic scale [52] (Figure 1A), and targeting ligands can be added at specific locations on the structure by using both chemical and genetic methods [50, 53]. In addition, CCMV has served as a model for implementing several novel approaches aimed at spatial control of multiligand presentation (Figures 1B and 1C) [38, 54].

Biofilms consist of localized, dense communities of organisms of a specific cell type growing amidst

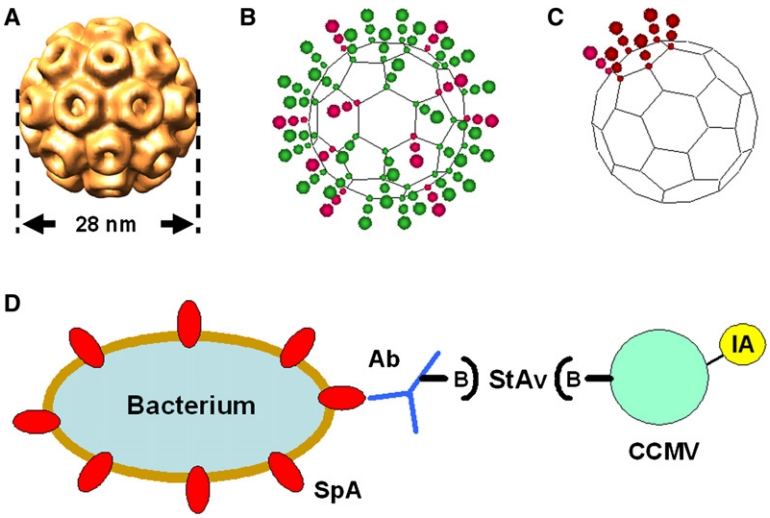

Figure 1. CCMV as a Multifunctional Nanoplatform

(A) Cryoreconstruction of CCMV.

(B and C) Schematic representations showing previous development of CCMV as a scaffold for design of multiligand presentation. (B) Functionalization with multiple ligands [53], including stoichiometric control of multiligand presentation [54]. (C) Asymmetric functionalization [38].

(D) Cartoon showing the strategy used to target CCMV to *S. aureus*; streptavidin (StAv) was used to couple biotinylated anti-SpA antibody (Ab) to CCMV, which was dual labeled with biotin (B) and an imaging agent (IA).

endogenous tissue. In this respect, they resemble tumors. Nanoparticles accumulate at sites of solid tumors and inflammation by extravasation facilitated by locally enhanced vascular permeability [55, 56]. The advantages gained from using nanoplatforms to deliver antimicrobials to biofilms have been demonstrated by the success obtained with immunoliposomes [57]. Biofilm cells are enclosed in a matrix of extracellular polymeric substances (EPSs) [58]. A concern that can be addressed by in vitro systems is whether a particular nanoplatform can penetrate through the EPS matrix to the cells [59].

In general, bacterial pathogens offer a plethora of targets for which a specific affinity ligand can be either discovered or engineered. *S. aureus*, a model organism for biofilm studies, expresses a variety of surface proteins involved in adhesion to host tissues and immune avoidance that can serve as specific molecular targets [60]. Among these is protein A (SpA), which binds to the Fc region of IgG and, thereby, may serve to conceal the cells from immune detection [61]. Here, we characterized the density and arrangement of functionalized CCMV particles targeted to SpA on *S. aureus* cells, assessed its capacity to deliver MRI contrast agent (CA) to *S. aureus* cells, and imaged the extent of its diffusive transport into an *S. aureus* biofilm. The results demonstrate that this multifunctional nanoplatform has potential for treating and diagnosing biofilm infections.

RESULTS

Targeting to *S. aureus*

The general targeting strategy consisted of using streptavidin (StAv) to couple biotinylated CCMV (CCMV-B) to biotinylated anti-SpA monoclonal antibody (anti-SpA mAb-B) that was bound to SpA expressed on the surface of *S. aureus* cells (Figure 1D). Briefly, the cells were first exposed to anti-SpA mAb-B, then to StAv, and finally to CCMV-B. Similar pretargeting strategies have been discussed in regard to radionulcide delivery for medical imaging [62]. In preliminary experiments, we used flow cytometry to verify that the anti-SpA mAb-B bound specifically to SpA presented on *S. aureus* under our experimental conditions (Figure S1; see the Supplemental Data available with this article online). For characterization of targeting by flow cytometry and epi-fluorescence microscopy, CCMV-B was fluorescently tagged with fluorescein (CCMV-B-F). Analysis by flow cytometry indicated that binding of CCMV-B-F to *S. aureus* cells was mediated specifically by the engineered interactions, and not by nonspecific binding of CCMV-B-F to components of the *S. aureus* cell wall (Figures 2A–2E). Negligible levels of binding were measured for *S. aureus* strain ATCC 12598 exposed only to CCMV-B-F (Figure 2B), and for *S. aureus* strain ATCC 10832, which does not express SpA, exposed only to CCMV-B-F (Figure 2D) or to anti-SpA mAb-B, StAv, and CCMV-B-F (Figure 2E). Epi-fluorescence microscopy was used to verify that the fluorescent objects detected by flow cytometry when CCMV-B-F was targeted to *S. aureus* ATCC 12598 were indeed cells exhibiting the expected morphology (Figure 2F).

High-Density Coverage of *S. aureus* Cells

Examination of *S. aureus* cells targeted with CCMV-B by both transmission electron microscopy (TEM) and field emission scanning electron microscopy (FESEM) indicated a high density of viral binding to the cell wall. TEM thin sections revealed that intact viral particles were arranged in a loosely packed dual layer around the cell periphery (Figures 3A–3C). Particles in TEM images were counted, yielding a mean of 60 particles per micrometer around the circumference of a planer section of a cell, or 1.6 monolayers if one monolayer is considered to consist of virus particles closely packed end to end. In a negative control experiment, no viral particles were associated with *S. aureus* cells exposed only to CCMV-B (Figure 3D; Figure S2), thus corroborating the interpretation that the extent of nonspecific binding of CCMV-B to *S. aureus* cells was negligible.

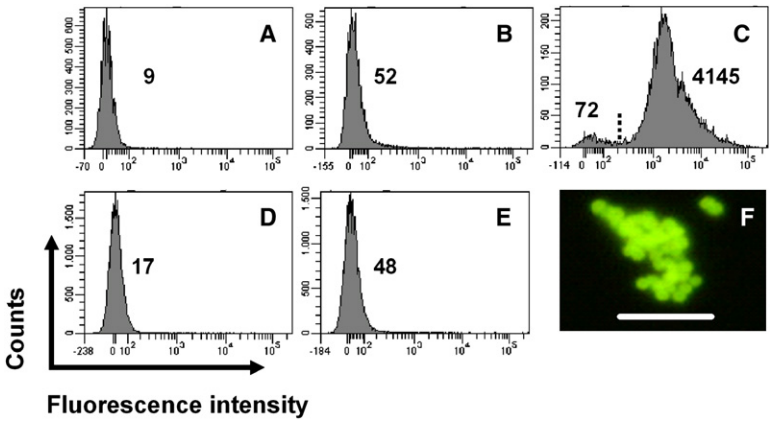

Figure 2. Flow Cytometry and Epi-Fluorescence Microscopy Indicating Specific Targeting of CCMV to *S. aureus* Cells

(A–E) Flow cytometry results. Numbers are mean fluorescence values; separate values are given for the two distinct features in (C). The four plots grouped on the left side ([A], [B], [D], and [E]) are negative controls. Results from two strains are shown. (A–C) ATCC 12598 (SpA positive): (A) cells only; (B) cells exposed to CCMV-B-F; (C) cells reacted with anti-SpA mAb-B then StAv and exposed to CCMV-B-F. (D and E) ATCC 10832 (SpA negative): (D) cells exposed to CCMV-B-F; (E) cells reacted with anti-SpA mAb-B then StAv and exposed to CCMV-B-F.

(F) Epi-fluorescence micrograph of a cluster of ATCC 12598 cells and a doublet from the preparation used to obtain results presented in (C); most of the cells were in fact singlets or doublets. There were no fluorescent objects that did not have the typical spherical shape of cocci. Unlabelled cells were not visible by using these acquisition parameters. The scale bar is 5 μm.

FESEM was used to further characterize the distribution of CCMV-B bound to SpA on the cell wall (Figure 4). Cells were densely covered with spherical particles over most of their visible surface area, as shown in Figures 4A–4C. Spherical particles that could be clearly distinguished were 28 nm in diameter, as expected for the CCMV capsid (Figure 4C) [52]. Viral particles in a number of densely covered areas, 200 × 200 nm^2 in size, and for which individual particles could be clearly distinguished, were counted, yielding a mean coverage of 1950 (SD 215) particles per μm^2 for these areas (see Figure S3). Combining enumerations of areal density based on both TEM and FESEM data yields 1.6 × 1950 (SD 215) or 3120 (SD 344) particles per μm^2 in densely covered regions of the cell wall. Thus, the arrangement of viral particles in more than one planar shell allows them to achieve a surface coverage that is 2.7 times the density of a hexagonally packed, planar array (1150 particles per μm^2). Qualitatively, regions exhibiting dense coverage of virus particles were present on every cell among the 30 observed (Figure S4). Typically, there were patches that were variable in size and shape that appeared to be completely devoid of particles, probably due to a lack of SpA in these regions. However, if this high density of coverage could be attained for the entire cell surface, $\sim 10^4$ particles could be targeted to a typical *S. aureus* cell with a diameter of 1 μm.

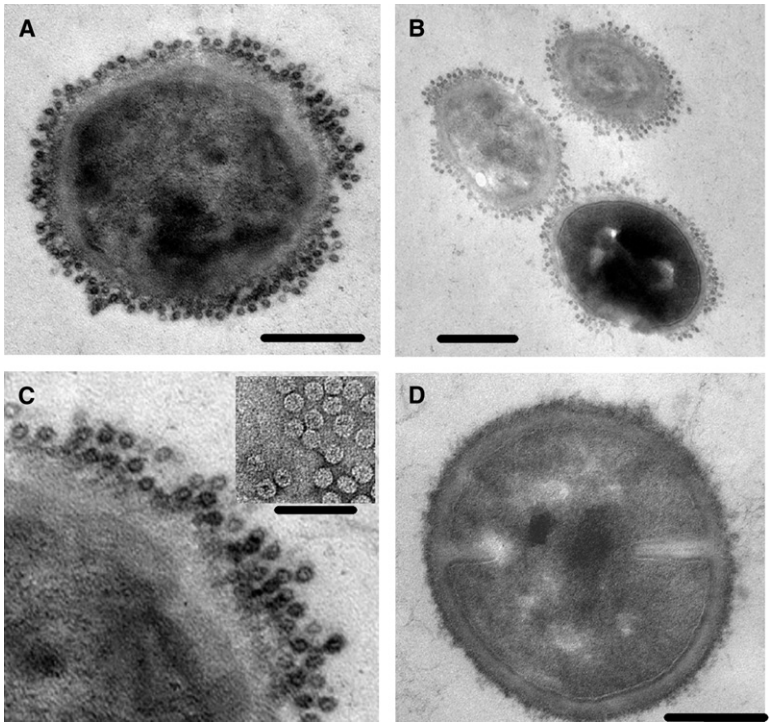

Figure 3. TEM Thin Sections Showing High-Density Coverage of CCMV Targeted to *S. aureus* Cells

(A and B) CCMV-B bound to *S. aureus* cells via the StAv/anti-SpA mAb-B linkage. The scale bars in (A) and (B) are 200 nm and 400 nm, respectively.

(C) Magnified view of image presented in (A) with an insert of a TEM image of CCMV-B adsorbed on Formvar presented at the same scale as the thin section. The scale bar is 100 nm.

(D) Representative image of an *S. aureus* cell from the negative control indicating a negligible level of nonspecific binding. The scale bar is 200 nm.

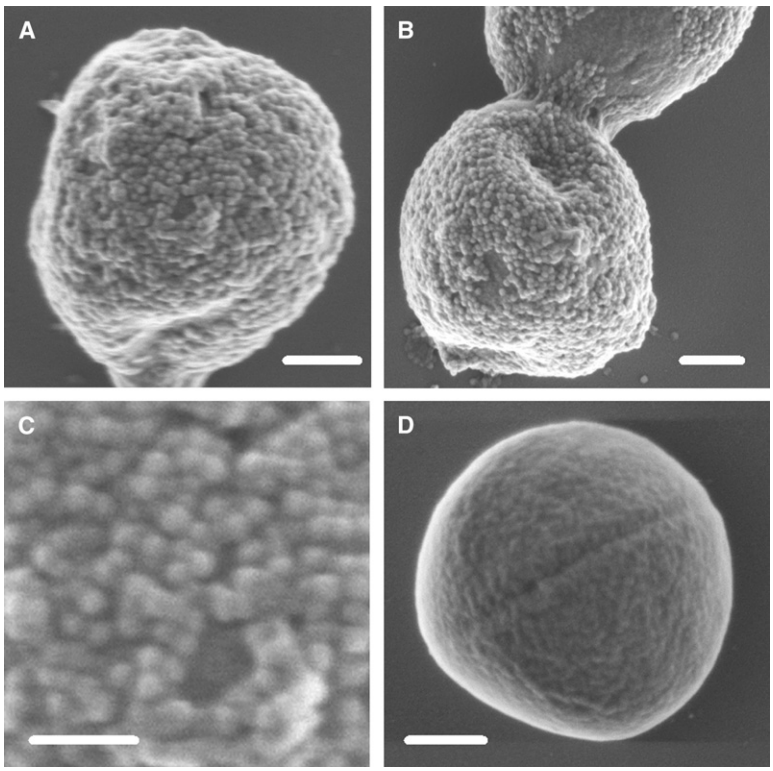

Figure 4. FESEM Images Showing High-Density Coverage of CCMV Targeted to *S. aureus* Cells

(A–D) (C) is a magnified view of the image presented in (A); (D) is an untargeted cell. The scale bars are 200 nm in (A), (B), and (D) and 100 nm in (C).

Targeted Delivery of an MRI Contrast Agent to *S. aureus* Cells

We used the multifunctional nanoplatform described above to target MRI CA to *S. aureus* cells. We first dual functionalized CCMV with both DOTA, a Gd(III)-chelating agent, and biotin. (This construct is referred to hence forth as CCMV-B-Gd.) Characterization by liquid chromatography/electrospray mass spectrometry (LC/MS) indicated that both DOTA and biotin functional groups were covalently linked into the CCMV-B-Gd construct, with some subunits functionalized with both groups (see Figure S5). The mean number of Gd ions chelated to the CCMV-B-Gd construct was estimated to be 166 per virion from these data (Table 1). The scheme outlined in Figure 1D was used to target CCMV-B-Gd to *S. aureus* cells. Analysis with inductively coupled plasma mass spectrometry (ICP-MS) to determine the concentration of Gd in a cell sample of known cell density indicated a value of 1.8×10^5 Gd atoms per cell. Assuming that the combined TEM and FESEM data yield a maximum estimate for the amount of CCMV that can be specifically targeted to the *S. aureus* cell wall by using our method, optimal targeting of the CCMV-B-Gd construct to the entire cell population would increase Gd loading by about an order of magnitude.

Targeting an *S. aureus* Biofilm

We used scanning laser confocal microscopy (SLCM) to image targeting of CCMV-B-F to an *S. aureus* biofilm (Figure 5). In preliminary experiments, we confirmed that ATCC strain 29213, known to be SpA positive [63], a biofilm former [64], and capable of inducing device-related infections in an animal model [65], expressed SpA in a

Table 1. Functional Group and Gd Abundance on CCMV-B-Gd

Functional Group(s)[a]	LC/MS[b]	Group(s)/CCMV[c]	Gd/Group[d]	Gd/Group (per CCMV)[e]
None	0.24	44	0	0
DOTA	0.05	8	0	0
B	0.06	12	0	0
DOTA-Gd	0.25	45	1	45
2B	0.04	8	0	0
B, DOTA-Gd	0.12	21	1	21
2(DOTA-Gd)	0.10	18	2	36
B, 2(DOTA-Gd)	0.06	11	2	22
3(DOTA-Gd)	0.08	14	3	42

[a] Functional group(s) on monomer subunit (abbreviations are in text), e.g., B, 2(DOTA-Gd) means a monomer functionalized with one biotin group and two DOTA groups, each chelating a Gd atom.
[b] Relative peak height from LC/MS data.
[c] Mean number of functional group(s) of each type (or combination) per virus particle.
[d] Number of Gd atoms per each functional group(s).
[e] Mean number of Gd atoms per each functional group per virus particle.

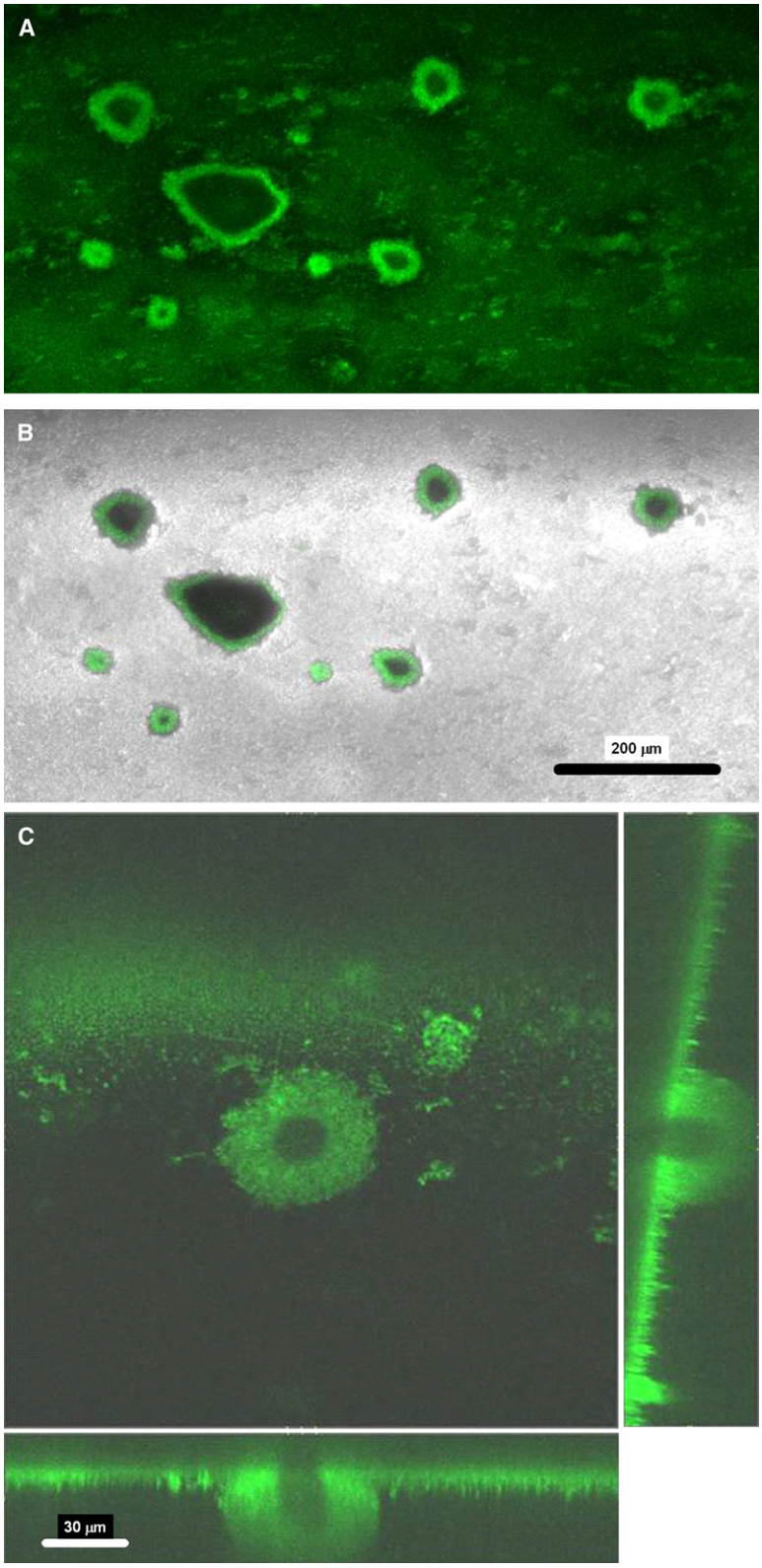

Figure 5. Penetration of Fluorescently Labeled CCMV into an *S. aureus* Biofilm

(A–C) SLCM images of microcolonies of an *S. aureus* biofilm reacted with anti-SpA mAb-B then StAv and exposed to CCMV-B-F for 80 min and rinsed. (A) Image of the fluorescence from CCMV-B-F that penetrated into the outer layer of biofilm microcolonies. (B) Overlay of the fluorescent image in (A) and an image of the same location taken in transmission mode. The scale bars in (A) and (B) are 200 μm. (C) Section through a microcolony at higher magnification; constructed sagittal sections are shown on the right side and bottom. The scale bar is 30 μm.

membrane biofilm model (Figure S6) and also in biofilms cultured in the flow cell (see Figure S7). To target CCMV to biofilm cells, ATCC strain 29213 biofilms were exposed sequentially to anti-SpA mAb-B, StAv, and CCMV-B-F to implement the targeting scheme outlined in Figure 1D. The extent of penetration of the nanoplatform into

S. aureus biofilm microcolonies was estimated by measuring the width of the fluorescence band that forms a ring bordering the periphery of microcolonies. The means of the maximum and minimum distances were obtained for each of 15 microcolonies, yielding an overall mean distance of penetration of 17.6 (SD 3.3) μm. In order to confirm that the sharp transitions between light and dark regions of fluorescence that were apparent to the eye were in fact real, line profiles of fluorescence intensity versus distance were computed for three microcolonies obtained at higher magnification. A representative line profile is shown in Figure S8A. These results demonstrate that this nanoplatform, which is quite massive on a molecular scale (~4×10^6 Da), can be used to target cells enclosed in the biofilm matrix. The clinical relevance is discussed below.

DISCUSSION

Our results demonstrate the ability to obtain targeting combined with a high-density of binding of a multifunctional protein cage nanoplatform to *S. aureus*. A previous study obtained more sparse coverage for binding of gold nanoparticles to *S. aureus* by using a similar targeting scheme [33]. In this study, a clinical isolate was used, whereas for studies here we used a strain known to express SpA at a high level. With appropriate manipulation of ligand presentation, constraints imposed on the binding density by the level of expression of one cell wall protein should not be a major caveat. *S. aureus* expresses at least 22 different cell wall-anchored proteins, many of which are involved in conferring virulence and are likely to be expressed at a high level in infections [60, 66]. CCMV and other similar protein cage architectures offer exceptionally versatile nanoplatforms for manipulating ligand presentation [53, 54, 67, 68]. This capacity can be exploited to cater the arrangement and composition of multiple ligands to optimize targeting to the large array of available surface proteins expressed by pathogenic *S. aureus* strains. The implication is that the high density of targeting demonstrated here can be achieved against a variety of *S. aureus* pathogens.

Protein cages have been shown to provide ideal architectures for the design of delivery vehicles that carry both therapeutic drugs [34] and imaging agents [35, 69]. Current techniques for imaging loci of infection are based primarily on nuclear medicine [70]. However, the development of nanoplatforms that specifically target high payloads of a CA to specific cell types is transforming MRI into a technique that can be used not only to resolve details of tissue morphology [71], but to obtain spatially resolved information about the molecular composition of tissues [72]. Since biofilm infections consist of regions densely populated with a distinct cell type, they are ideal candidates for imaging via CA-enhanced MRI. Dual-functionalized CCMV enabled targeted delivery of 1.8×10^5 Gd atoms per cell. This level of Gd loading onto *S. aureus* cells would result in ~10 μM Gd chelate in a typical *S. aureus* biofilm in which the distance between cells is less than 3 μm [73] (~3×10^{10} cells/ml). For a Gd chelate with a relaxivity (longitudinal relaxation rate normalized to Gd chelate concentration) of about 4 $mM^{-1}s^{-1}$, it has been estimated that ~50 μM Gd chelate is required for discrimination of tissues targeted with MRI CA [74]. Assuming that there is no nonspecific labeling of nontargeted tissue, the concentration of Gd chelate required for discrimination of tissues targeted with CA is inversely proportional to the relaxivity [74]. Gd acquires a greatly increased relaxivity when it is bound to the relatively rigid CCMV scaffold [69], indicating that a concentration of only 1 μM Gd may be sufficient to discriminate *S. aureus* biofilms targeted with CCMV-Gd from surrounding tissue at a Larmor frequency of 50 MHz. In addition, previous results suggest that Gd loading onto CCMV can be increased substantially [53]. Furthermore, our results here indicate that loading of CCMV onto *S. aureus* cells can be increased by perhaps an order of magnitude. Taken together, these considerations suggest that multifunctional nanoplatforms based on protein cage architectures will yield potent infection-specific MRI imaging probes that can be used to identify and characterize loci of biofilm infection.

The optimal multifunctional platform should be relatively large—on a molecular scale—thus enabling it to target a substantial payload to specific cell types, but sufficiently small to allow efficient transport into biofilms. As the targeted epitopes presented in the cell wall become more sparse than the footprint of a smaller targeting molecule such as an antibody, the loading advantage approaches the ratio of their molecular weights, yielding an ~25 times advantage in potential cellular loading capacity for the CCMV nanoplatform compared to an IgG molecule. Biofilm cells are enclosed in a matrix of EPS [58], which, at least from an intuitive standpoint, seems likely to significantly impede transport of these relatively large nanoplatforms. In addition, the cellular density of *S. aureus* biofilms is quite high.

Our results indicate that CCMV penetrated into an *S. aureus* biofilm ~20 μm during an 80 min exposure (0.25 μm/min). Despite its large size, a higher rate of transport of CCMV into the biofilm could be anticipated. Based on its diffusion coefficient in aqueous solution [51], CCMV can penetrate a boundary layer 100 μm thick (reaching 90% of the bulk concentration) within ~11 min (Figure S8C). The decrease in the rate of diffusive transport of molecules by interaction with biofilm components has been described by an effective diffusion coefficient [75]. For molecules within the size range of CCMV, this effective diffusion coefficient is 10–20 times less than its aqueous counterpart. This translates to an estimate of ~10–20 min to penetrate a microcolony such as that shown in Figure 5C. It is possible that the viral protein cage penetrated farther than 20 μm into the biofilm microcolonies, and that it was unable to bind to cells due to a lack of SpA expression in the interior of the microcolonies and, consequently, was removed from these inner regions by diffusive transport during the time interval between the last rinse step and the SLCM measurement (~3 hr).

SpA expression may have been influenced by a microenvironment such as reduced oxygen that is likely to have developed in central regions of the microcolonies [76]. In support of this alternative interpretation, the distribution of fluorescence with respect to distance along the substratum shows a transition between light and dark regions that is quite abrupt and thus not compatible with the description provided by a simple model of diffusive transport (Figures S8A and S8D).

The rate of diffusive transport of a substance through a biofilm cannot be predicted based exclusively on its size, which is the primary factor governing its transport in aqueous medium. In general, the rate of transport of nanoplatforms into biofilms is expected to be significantly altered by their surface properties, since this will influence sorption to biofilm components [75]. Liposomes incorporating phosphatidylinositol or functionalized with PEG fully penetrated to the base of a 20 μm thick *S. aureus* biofilm during a 2 hr exposure period, while other cationic liposomes adsorbed only to the outer layers [59]. Thus, binding of targeted CCMV nanoplatforms to cells is likely to have hindered their transport through the biofilm to some degree.

Even penetration into a biofilm by a nanoplatform to a distance of 20 μm may be sufficient to target the majority of cells in most biofilm infections. With the exception of two early studies [77, 78], there is a paucity of information on the structure of in vivo biofilms associated with biomaterial-centered infections in humans. *S. aureus* biofilms involved in a catheter infection in a mouse model colonized to an areal density of $\sim 3 \times 10^7$ cells/cm^2, which would yield a nominal thickness of 10 μm for an *S. aureus* biofilm with a similar cell density as our in vitro biofilm [79]. An *S. aureus* biofilm of similar dimensions was obtained on an implanted tissue cage in a guinea pig model [80], while micrographs of osteomyelitis induced in a rat model from a precolonized implant indicated an *S. aureus* biofilm of smaller dimensions [81]. If these studies are representative of the type of *S. aureus* biofilms involved in human infections, our results indicate that a nanoplatform approximately the same size as CCMV could penetrate to all of the cells in a biofilm infection within a 2 hr exposure period.

Our results, together with estimates for transport of very large molecules through biofilms discussed briefly, suggest that the limiting factor in developing multifunctional nanoplatforms based on protein cage architectures for diagnosis and treatment of biofilm infections is not likely to be the rate of penetration into the biofilm matrix. A rough estimate of the plasma half-life that is necessary for effective penetration to an extravascular site can be obtained from extensive studies of nanoplatforms used to diagnose and treat cancer. Liposomes sterically stabilized with PEG and incorporating doxorubicin (SSL DOX), which are among the most promising delivery vehicles for anticancer agents, have plasma half-lives in humans of ~50 hr [82]. Ferumoxtran-10, a superparamagnetic iron oxide nanoparticle used to enhance MRI visualization of lymphomas, has a half-life of between 24 and 30 hr [83]. Placed in the perspective of residence times in the circulatory system of between 24 and 50 hr, the time of about 2 hr required to penetrate a 30 μm thick biofilm is probably not the factor that will limit application of this technology.

A fundamental issue that needs to be addressed before nanoplatforms based on protein cage architectures can be used for clinical applications is the response of the immune system. CCMV did not elicit a hypersensitive response when injected intravenously into mice and was distributed to a variety of tissues, indicating its ability to extravasate from the vascular system [84]. However, the rate of clearance from the circulatory system was rapid and might preclude passive or active targeting. The clinical application of superparamagnetic iron oxide nanoparticles was enabled primarily by the development of surface modifications that increased the plasma half-life [85]. As with liposomal systems, derivatization with PEG holds promise as a means of modulating the immune response to viral-based nanoplatforms [86].

SIGNIFICANCE

New approaches are required to effectively diagnose and treat persistent infections that are recalcitrant to conventional antimicrobial therapies. Our results indicate that multifunctional nanoplatforms based on targeted protein cage architectures have significant potential for treating and diagnosing localized infections. In this respect, two key functional attributes were demonstrated. First, the density of binding of targeted CCMV to a surface protein expressed by *S. aureus* was exceptionally high. Second, CCMV penetrated into an *S. aureus* biofilm at a rate that was rapid enough to make clinical applications feasible. The multifunctional platform that we used for these studies is an ideal system for catering ligand presentation to optimize targeting to a variety of surface proteins expressed by pathogenic bacteria, or to combinations of these proteins. In turn, the size range of these nanoplatforms potentiates targeted delivery of large payloads of imaging agents or therapeutic drugs to loci of infections. In short, versatile multifunctional nanoplatforms such as these offer a template upon which the chemist and biologist can structure innovative approaches to infection control.

EXPERIMENTAL PROCEDURES

Antibody

Anti-SpA mAb was produced in mouse (clone SPA-27) and was biotinylated by the supplier (P3150 Sigma-Aldrich Co.) It was raised against the Cowan I strain and binds to an epitope that is distinct from the Fc-binding region.

Bacterial Strains and Culturing

ATCC strains 12598 (Cowan I, SpA +), 10832 (Wood 46, SpA −), and 29213 (SpA +, biofilm former) were used for these studies. Planktonic cells were grown in batch cultures in nutrient broth for 8 hr at 37°C. Biofilms of 29213 were cultured in tryptic soy broth (TSB) diluted 1:10 with nanopure water at 37°C in a square, glass flow cell similar

to a system used previously to characterize *S. aureus* biofilms [73]. Biofilms were cultured for between 5 and 7 days, until there was visible growth in the tube.

Virus Preparation and Functional Group Addition

CCMV was isolated from cowpea plants as previously described [87]. Purity was verified by using size-exclusion chromatography (SEC) and dynamic light scattering (DLS) [88]. Protein concentration was determined by using the absorbance at 260 nm [51]. CCMV was biotinylated by reaction of a 0.5 mM solution of sulfosuccinimidyl-6′-(biotinamido)-6-hexanamido hexanoate (Pierce) with 0.4 μM (1.4 mg ml^{-1}) CCMV in 50 mM HEPES buffer, 150 mM NaCl (pH 7.0) at room temperature with stirring for 30 min. The reaction was terminated by exchange into 1 mM sodium acetate buffer (pH 4.8) by using SEC (Superose 6, Amersham Biosciences, Uppsala, Sweden). Fractions eluting from within the CCMV peak, the position of which was predetermined by using unlabeled CCMV, were used for the experiments. These reaction conditions were predetermined to leave some reactive amines on lysine groups available for fluorescent tagging. Labeled virus was further purified by dialysis into 100 mM sodium acetate buffer. The integrity of the labeled virus was confirmed by DLS and TEM as described previously [88]. Association of biotin with the virus was initially tested by a dot blot assay by using alkaline phosphatase-conjugated anti-biotin antibody (A-7064, Sigma), and covalent attachment to protein monomer subunits was verified by liquid chromatography/electrospray mass spectrometry (LC/MS). Biotin-conjugated CCMV (CCMV-B) was tagged with fluorescein by reaction of a 0.5 mM solution of 5-(and-6)-carboxyfluorescein, succinimidyl ester (Sigma-Aldrich) with 3.0 mM (1.4 mg ml^{-1}) CCMV in 50 mM HEPES buffer, 150 mM sodium chloride (pH 7.0) at room temperature with stirring for 60 min. The reaction was terminated by dialysis into 1 mM sodium acetate buffer (pH 4.8). CCMV/K42R, an exceptionally stable genetic construct [89], was dual functionalized with a Gd chelate (DOTA, Macrocyclics, B-280) and biotin by first reacting the protein cage with DOTA, then chelating the Gd to the DOTA-functionalized CCMV, and, finally, biotinylating this product by following the protocol described above. CCMV/K42R was functionalized with DOTA by reaction with an NHS ester of DOTA in 100 mM HEPES, 100 mM sodium chloride (pH 7.2) (reaction buffer) by using a final molar ratio of 20:1 of the DOTA reagent:CCMV/K42R monomer subunit. The DOTA reagent was added into a 2 mg/ml CCMV/K42R solution in increments of ~5 mg, while alternately maintaining the pH at 7.2 by titrating in 0.5 M sodium hydroxide, and was allowed to react until completion, which was determined by using LC/MS to monitor the progress of the reaction. The reaction was terminated by dialysis into 100 mM HEPES, 100 mM sodium chloride (pH 6.5) (storage buffer) overnight. After dialysis, the preparation was centrifuged (17,900 × g) for 5 min, and the supernatant was dialyzed against a solution of Gd in the reaction buffer; Gd concentration was adjusted to be 10× the DOTA chelate concentration. LC/MS was used to follow the reaction to completion, and then the reaction was terminated by exchange into the storage buffer by using SEC (Superose 6, Amersham Biosciences, Uppsala, Sweden). Multiple buffer exchanges were carried out to rid the sample of unbound Gd, and then the CCMV/K42R functionalized with DOTA-Gd was labeled with biotin as described above. LC/MS was used to quantify the extent of DOTA-Gd, DOTA, and biotin conjugation to CCMV/K42R. A functional assay was performed in order to determine the availability of the biotin functional groups on CCMV-B-Gd for binding to StAv (Figure S9). The construct is quite stable, probably due to the K42R background. After 1 year of storage, the construct preparation maintained ~80% of its Gd load (ICP analysis) and was used to target cells with intact virus particles (FESEM analysis) (Figure S10).

Targeting *S. aureus* Planktonic Cells

We modified protocols previously published to bind antibody to the cells and then StAv to the antibody-coated cells [90, 91]. Cells were pelleted at 2500 × g for 10 min at 4°C and resuspended in 5% bovine calf serum (VWR), 0.1% intravenous immune globulin (Genesis BioPharmaceuticals), 0.02% sodium azide in PBS (10 mM sodium phosphate, 100 mM sodium chloride [pH 7.2]) for 1 hr. The solution was then incubated for 30 min at 4°C with a 1:1000 dilution of biotinylated anti-SpA mAb-B. Cells were washed twice in 2% bovine calf serum and 0.02% sodium azide in PBS (wash solution). A portion of the washed cells was reacted with ExtrAvidin-R-Phycoerythrin (Sigma-Aldrich) (10 μl of the solution from the supplier in 1 ml wash solution for 30 min at 4°C) to verify expression of SpA for the negative controls (or lack of SpA expression in the case of the Wood 46 strain). A portion of the washed cells was reacted with StAv (Sigma-Aldrich) (50 μg/ml in wash solution) and incubated for 30 min at 4°C. Cells were washed once in wash solution and then twice in 0.02% sodium azide in PBS. CCMV-B, CCMV-B-F, or CCMV-B-DOTA-Gd was added at between 130 and 210 μg/ml to the cell pellet in PBS at pH 6.7 and then incubated for 30 min at 4°C. Cells labeled with CCMV-B-F were analyzed immediately after this last step by using flow cytometry. Before ICP analysis, cells were washed four times in 1 ml PBS to dilute the CCMV/K42R-DOTA-Gd-B by a factor of greater than 10^{-4}, leaving a Gd concentration remaining from the unbound protein cage of less than 1 picomolar. For TEM preparations and ICP analysis, cells were fixed in 3% gluteraldehyde. For microscopic analysis, cells were fixed in 1% paraformaldehyde in PBS. Negative controls consisted of the same steps, but without addition of the antibody.

Targeting of Biofilm

At the end of the growth period, the capillary tube with the *S. aureus* biofilm and silicone leader tubing was removed from the reactor system by clamping and cutting the tubing. The biofilm was exposed to different solutions by using a syringe connected to the effluent tubing to draw solutions into the capillary via the influent tubing. The biofilm was rinsed with 1 ml TSB with 0.02% sodium azide (TSB-NaN_3) and then exposed to a 1:100 dilution of anti-SpA mAb-B in TSB-NaN_3 for 1 hr. This was followed by another rinse with 1 ml TSB-NaN_3 and exposure to 100 μg/ml StAv (or fluorescein-tagged StAv [StAv-F] [Sigma-Aldrich]) in TSB-NaN_3 for 1 hr to obtain results presented in Figure S7). After another rinse with 1 ml TSB-NaN_3, the biofilm was exposed to CCMV-B-F at 130 μg/ml for 80 min in PBS (pH6.7) and then rinsed with 1 ml TSB-NaN_3. Finally, the biofilm was exposed to 1% paraformaldehyde in PBS (pH 6.7). (The residual volume of the capillary flow cell and leader tubing was ~0.2 ml for each experiment.) Approximately 3 hr elapsed between the SCLM viewing of the biofilm and the last rinse step.

Flow Cytometry

Fluorescence from cells was analyzed by using the BD FACSAria cell sorter (BD BioSciences). Side scatter was used to threshold the signal. Optical parameters were: excitation, 488 nm; emission, 575/26 for phycoerythrin and 530/30 for fluorescein.

Transmission Electron Microscopy

Cells were centrifuged at low speed to form a pellet, and a few drops of 2% noble agar were added just before hardening. The pellet was briefly mixed and allowed to harden, cut into smaller pieces, and fixed overnight with 3% gluteraldehyde in potassium sodium phosphate buffer (PSPB [pH 7.2]). Agar pieces were then washed three times with PSPB for 10 min, postfixed in 2% osmium tetroxide at room temperature for 4 hr, dehydrated in an ethanol series, dissolved in propylene oxide, gradually infiltrated with Spurr's resin [92], and baked overnight at 70°C. Thin sections, 60–90 nm, were cut with a Diatome diamond knife on a Reichert OM-U2 ultramicrotome. Sections were floated onto 300 mesh copper grids and stained with uranyl acetate and Reynold's lead citrate [93] Negatively stained virus particles were prepared by placing 5 μl purified virus on a carbon-stabilized, formvar-coated 300 mesh copper grid and staining it with 2% UA in water. All grids were viewed with a LEO 912AB transmission electron microscope.

Field Emission Scanning Electron Microscopy

Cells fixed in gluteraldehyde were adsorbed to polylysine-coated Si < 100 > wafers (Virginia Semiconductor Inc., Fredericksburg, VA) by exposing the coupons to a cell suspension in 3% gluteraldehyde/PBS for 1 hr. The coupons were rinsed twice in Nanopure water and dried under a stream of liquid nitrogen. The coupons with adsorbed cells were coated with a thin film of iridium by exposing the sample for 15 s at 20 mA in an Emitech sputter coater. Cells were viewed with a Supra 55VP FESEM (Zeiss) by using the Inlens detector at 1 kV and 3 mm working distance.

Conventional Optical Microscopy

Epi-fluorescence images were acquired through a B2A filter block (excitation, 450–490 nm; emission, >515 nm) at 1000× (100× objective and 10× camera lens) by using a Nikon Eclipse E600 coupled to an Olympus Camedia camera. Cell counts were made in transmission mode at 400× (40× objective and a 10× ocular) by using a Zeiss Axioscope microscope to acquire images of the cells suspended in a known volume (10 μl) of PBS. The mean number of cells in 20 fields was used for the estimation of cell density.

Scanning Confocal Laser Microscopy

Confocal microscope images were collected on a Leica TCS-SP2-AOBS confocal with a 63× 0.9 NA HCX APO L U-V-I water-immersion objective. Fluorescein was excited with a 488 nm laser, and fluorescence was collected from 504 nm to 619 nm. Images were taken at 0.5 μm intervals throughout the depth of the biofilm, then stacks were combined in *Imaris* image analysis software (Bitplane AG, Zurich, Switzerland) to yield final images. Line profiles were obtained by using Image-Pro Plus (MediaCybernetics) software.

Liquid Chromatography/Electrospray Mass Spectrometry

LC/MS was performed on a QToF Micro instrument (Waters). CCMV injected at 50–100 μg ml^{-1} (1–10 μl) was eluted from a C-8 reverse-phase column (VYDAC) by using an acetonitrile/H_2O gradient in 0.1% formic acid. The virus disassembled in the running buffer into monomers that were analyzed by the detector. Mass spectra of the multiply charged ions were deconvoluted by using instrument software to produce a representation of monomer mass versus intensity. Monomers from labeled virus produced clearly separated peaks in these processed spectra with masses corresponding to the monomer mass and the monomer mass plus between one and three reacted reagent molecules (i.e., reagent molecules minus the sulfo-NHS ester leaving group). The relative peak height was used to determine the extent of labeling. This was converted to mean number of biotins, DOTA, and DOTA-Gd chelates per CCMV particle.

Inductively Coupled Plasma Analysis

An Agilent 7500ce inductively coupled plasma mass spectrometer (ICP-MS) was used to determine Gd concentration in the *S. aureus* cell preparation with bound CCMV/K42R-B-DOTA-Gd. A 1 ml cell preparation of 6.8 × 10^7 cells/ml was diluted to a volume of 5 ml in 2% nitric acid for this measurement. Interferences arising from the plasma and sample matrix were eliminated with an Octopole Reaction System (ORS), which is positioned between the source and the mass filter. A buffer solution and a solution containing Gd^{3+} were both used to optimize transmission of Gd ions while eliminating interfering species. A calibration curve was constructed by using a series of Gd standards with concentrations spanning the expected range of the sample. A blank was used in the analysis and was included in the calibration curve.

Supplemental Data

Supplemental data include flow cytometry results (Figure S1), TEM thin sections from the negative control (Figure S2), FESEM images of densely covered regions (Figure S3), SEM images of CCMV-B bound to *S. aureus* (Figure S4), an LC/MS spectrum of CCMV/K42R-DOTA-Gd-B (Figure S5), flow cytometry results (Figure S6), an SCLM image of a biofilm of *S. aureus* reacted with anti-SpA mAb and then StAv-F (Figure S7), quantitative analysis of confocal images (Figure S8), a functional assay testing the availability of the biotin functional groups on CCMV-B-Gd for binding to StAv (Figure S9), and FESEM images of CCMV-B-Gd targeted to cells, demonstrating the stability of this construct after long-term storage (Figure S10). These data are available online at http://www.chembiol.com/cgi/content/full/14/4/387/DC1/.

ACKNOWLEDGMENTS

This work was funded by grants from the National Institutes of Health (R01 EB00432), the Office of Naval Research for support of the Center for BioInspired Nanomaterials (19-00-R0006), and Montana Idea Network for Biomedical Research Excellence (MT INBRE) (M276-05W0021).

Received: October 20, 2006
Revised: January 10, 2007
Accepted: February 7, 2007
Published: April 27, 2007

REFERENCES

1. Costerton, J.W., Stewart, P.S., and Greenberg, E.P. (1999). Bacterial biofilms: a common cause of persistent infections. Science *284*, 1318–1322.
2. Walsh, C. (2000). Molecular mechanisms that confer antibacterial drug resistance. Nature *406*, 775–781.
3. Davies, J. (1996). Bacteria on the rampage. Nature *383*, 219–220.
4. Chen, I., Christie, P.J., and Dubnau, D. (2005). The ins and outs of DNA transfer in bacteria. Science *310*, 1456–1460.
5. Obritsch, M.D., Fish, D.N., MacLaren, R., and Jung, R. (2005). Nosocomial infections due to multidrug-resistant *Pseudomonas aeruginosa*: epidemiology and treatment options. Pharmacotherapy *25*, 1353–1364.
6. DeRyke, C.A., Maglio, D., and Nicolau, D.P. (2005). Defining the need for new antimicrobials: clinical and economic implications of resistance in the hospitalised patient. Expert Opin. Pharmacother. *6*, 873–889.
7. Coimbra, M.V.D., Silva-Carvalho, M.C., Wisplinghoff, H., Hall, G.O., Tallent, S., Wallace, S., Edmond, M.B., Figueiredo, A.M.S., and Wenzel, R.P. (2003). Clonal spread of methicillin-resistant *Staphylococcus aureus* in a large geographic area of the United States. J. Hosp. Infect. *53*, 103–110.
8. Gristina, A.G. (1987). Biomaterial-centered infection: microbial adhesion versus tissue integration. Science *237*, 1588–1595.
9. Braxton, E.E., Ehrlich, G.D., Hall-Stoodley, L., Stoodley, P., Veeh, R., Fux, C., Hu, F.Z., Quigley, M., and Post, J.C. (2005). Role of biofilms in neurosurgical device-related infections. Neurosurg. Rev. *28*, 249–255.
10. Hall-Stoodley, L., Costerton, J.W., and Stoodley, P. (2004). Bacterial biofilms: from the natural environment to infectious diseases. Nat. Rev. Microbiol. *2*, 95–108.
11. Fux, C.A., Costerton, J.W., Stewart, P.S., and Stoodley, P. (2005). Survival strategies of infectious biofilms. Trends Microbiol. *13*, 34–40.
12. Rice, L.B. (2006). Unmet medical needs in antibacterial therapy. Biochem. Pharmacol. *71*, 991–995.
13. Amaral, M.M., Coelho, L.R., Flores, R.P., Souza, R.R., Silva-Carvalho, M.C., Teixeira, L.A., Ferrerira-Carvalho, B.T., and Figueiredo, A.M.S. (2005). The predominant variant of the Brazilian epidemic clonal complex of methicillin-resistant *Staphylococcus aureus* has an enhanced ability to produce biofilm and to adhere to and invade airway epithelial cells. J. Infect. Dis. *192*, 801–810.

14. Ando, E., Monden, K., Mitsuhata, R., Kariyama, R., and Kumon, H. (2004). Biofilm formation among methicillin-resistant *Staphylococcus aureus* isolates from patients with urinary tract infection. Acta Med. Okayama *58*, 207–214.

15. O'Riordan, K., and Lee, J.C. (2004). *Staphylococcus aureus* capsular polysaccharides. Clin. Microbiol. Rev. *17*, 218–234.

16. Stefani, S., and Varaldo, P.E. (2003). Epidemiology of methicillin-resistant staphylococci in Europe. Clin. Microbiol. Infect. *9*, 1179–1186.

17. Parfitt, T. (2005). Georgia: an unlikely stronghold for bacteriophage therapy. Lancet *365*, 2166–2167.

18. Summers, W.C. (2001). Bacteriophage therapy. Annu. Rev. Microbiol. *55*, 437–451.

19. Wainwright, M., and Crossley, K.B. (2004). Photosensitising agents—circumventing resistance and breaking down biofilms: a review. Int. Biodeterior. Biodegradation *53*, 119–126.

20. Demidova, T.N., and Hamblin, M.R. (2004). Photodynamic therapy targeted to pathogens. Int. J. Immunopathol. Pharmacol. *17*, 245–254.

21. Ahmed, K., and Jones, M.N. (2003). The effect of shear on the desorption of liposomes adsorbed to bacterial biofilms. J. Liposome Res. *13*, 187–197.

22. Catuogno, C., and Jones, M.N. (2003). The antibacterial properties of solid supported liposomes on *Streptococcus oralis* biofilms. Int. J. Pharm. *257*, 125–140.

23. Hutchinson, F.J., and Jones, M.N. (1988). Lectin-mediated targeting of liposomes to a model surface. An ELISA method. FEBS Lett. *234*, 493–496.

24. Jones, M.N., Hill, K.J., Kaszuba, M., and Creeth, J.E. (1998). Antibacterial reactive liposomes encapsulating coupled enzyme systems. Int. J. Pharm. *162*, 107–117.

25. Jones, M.N. (2005). Use of liposomes to deliver bactericides to bacterial biofilms. Methods Enzymol. *331*, 211–228.

26. Kim, H.J., Gias, E.L.M., and Jones, M.N. (1999). The adsorption of cationic liposomes to *Staphylococcus aureus* biofilms. Colloids Surf. A-Physicochem. Eng. Asp. *149*, 561–570.

27. Svenson, S., and Tomalia, D.A. (2005). Dendrimers in biomedical applications—reflections on the field. Adv. Drug Deliv. Rev. *57*, 2106–2129.

28. Roy, I., Ohulchanskyy, T.Y., Pudavar, H.E., Bergey, E.J., Oseroff, A.R., Morgan, J., Dougherty, T.J., and Prasad, P.N. (2003). Ceramic-based nanoparticles entrapping water-insoluble photosensitizing anticancer drugs: a novel drug-carrier system for photodynamic therapy. J. Am. Chem. Soc. *125*, 7860–7865.

29. Gao, X., Cui, Y., Levenson, R.M., Chung, L.W., and Nie, S. (2004). In vivo cancer targeting and imaging with semiconductor quantum dots. Nat. Biotechnol. *22*, 969–976.

30. Harisinghani, M.G., Saini, S., Weissleder, R., Hahn, P.F., Yantiss, R.K., Tempany, C., Wood, B.J., and Mueller, P.R. (1999). MR lymphangiography using ultrasmall superparamagnetic iron oxide in patients with primary abdominal and pelvic malignancies: radiographic-pathologic correlation. AJR Am. J. Roentgenol. *172*, 1347–1351.

31. Anderson, S.A., Rader, R.K., Westlin, W.F., Null, C., Jackson, D., Lanza, C.M., Wickline, S.A., and Kotyk, J.J. (2000). Magnetic resonance contrast enhancement of neovasculature with α(v)β(3)-targeted nanoparticles. Magn. Reson. Med. *44*, 433–439.

32. Zheng, G., Chen, J., Li, H., and Glickson, J.D. (2005). Rerouting lipoprotein nanoparticles to selected alternate receptors for the targeted delivery of cancer diagnostic and therapeutic agents. Proc. Natl. Acad. Sci. USA *102*, 17757–17762.

33. Zharov, V.P., Mercer, K.E., Galitovskaya, E.N., and Smeltzer, M.S. (2006). Photothermal nanotherapeutics and nanodiagnostics for selective killing of bacteria targeted with gold nanoparticles. Biophys. J. *90*, 619–627.

34. Flenniken, M.L., Liepold, L.O., Crowley, B.E., Willits, D.A., Young, M.J., and Douglas, T. (2005). Selective attachment and release of a chemotherapeutic agent from the interior of a protein cage architecture. Chem. Commun. 447–449.

35. Flenniken, M.L., Willits, D.A., Harmsen, A.L., Liepold, L.O., Harmsen, A.G., Young, M.J., and Douglas, T. (2006). Melanoma and lymphocyte cell-specific targeting incorporated into a heat shock protein cage architecture. Chem. Biol. *13*, 161–170.

36. Douglas, T., and Young, M. (2006). Viruses: making friends with old foes. Science *312*, 873–875.

37. Douglas, T., and Young, M. (1998). Host-guest encapsulation of materials by assembled virus protein cages. Nature *393*, 152–155.

38. Klem, M.T., Willits, D., Young, M., and Douglas, T. (2003). 2-D array formation of genetically engineered viral cages on Au surfaces and imaging by atomic force microscopy. J. Am. Chem. Soc. *125*, 10806–10807.

39. Wang, Q., Kaltgrad, E., Lin, T.W., Johnson, J.E., and Finn, M.G. (2002). Natural supramolecular building blocks: wild-type cowpea mosaic virus. Chem. Biol. *9*, 805–811.

40. Khayat, R., Tang, L., Larson, E.T., Lawrence, C.M., Young, M., and Johnson, J.E. (2005). Structure of an archaeal virus capsid protein reveals a common ancestry to eukaryotic and bacterial viruses. Proc. Natl. Acad. Sci. USA *102*, 18944–18949.

41. Kramer, R.M., Li, C., Carter, D.C., Stone, M.O., and Naik, R.R. (2004). Engineered protein cages for nanomaterial synthesis. J. Am. Chem. Soc. *126*, 13282–13286.

42. Okuda, M., Kobayashi, Y., Suzuki, K., Sonoda, K., Kondoh, T., Wagawa, A., Kondo, A., and Yoshimura, H. (2005). Self-organized inorganic nanoparticle arrays on protein lattices. Nano Lett. *5*, 991–993.

43. Scheybani, T., Yoshimura, H., Baumeister, W., and Nagayama, K. (1996). Stabilization of a fragile two-dimensional protein crystal at the water-air interface: the square lattice of apoferritin. Langmuir *12*, 431–435.

44. Yamashita, I. (2001). Fabrication of a two-dimensional array of nano-particles using ferritin molecule. Thin Solid Films *393*, 12–18.

45. Gilles, C., Bonville, P., Rakoto, H., Broto, J.M., Wong, K.K.W., and Mann, S. (2002). Magnetic hysteresis and superantiferromagnetism in ferritin nanoparticles. J. Magn. Magn. Mater. *241*, 430–440.

46. Flenniken, M.L., Willits, D.A., Brumfield, S., Young, M.J., and Douglas, T. (2003). The small heat shock protein cage from *Methanococcus jannaschii* is a versatile nanoscale platform for genetic and chemical modification. Nano Lett. *3*, 1573–1576.

47. McMillan, R.A., Howard, J., Zaluzec, N.J., Kagawa, H.K., Mogul, R., Li, Y.F., Paavola, C.D., and Trent, J.D. (2005). A self-assembling protein template for constrained synthesis and patterning of nanoparticle arrays. J. Am. Chem. Soc. *127*, 2800–2801.

48. Wiedenheft, B., Mosolf, J., Willits, D., Yeager, M., Dryden, K.A., Young, M., and Douglas, T. (2005). An archaeal antioxidant: characterization of a Dps-like protein from *Sulfolobus solfataricus*. Proc. Natl. Acad. Sci. USA *102*, 10551–10556.

49. Resnick, D.A., Gilmore, K., Idzerda, Y.U., Klem, M.T., Allen, M., Douglas, T., Arenholz, E., and Young, M. (2006). Magnetic properties of Co3O4 nanoparticles mineralized in *Listeria innocua* Dps. J. Appl. Phys. *99*, 08Q501.

50. Douglas, T., Strable, E., Willits, D., Aitouchen, A., Libera, M., and Young, M. (2002). Protein engineering of a viral cage for constrained nanomaterials synthesis. Adv. Mater. *14*, 415–418.

51. Bancroft, J.B., Hiebert, E., Rees, M.W., and Markham, R. (1968). Properties of cowpea chlorotic mottle virus, its protein and nucleic acid. Virology *34*, 224–239.

52. Speir, J.A., Munshi, S., Wang, G.J., Baker, T.S., and Johnson, J.E. (1995). Structures of the native and swollen forms of cowpea chlorotic mottle virus determined by X-ray crystallography and cryoelectron microscopy. Structure *3*, 63–78.

53. Gillitzer, E., Willits, D., Young, M., and Douglas, T. (2002). Chemical modification of a viral cage for multivalent presentation. Chem. Commun. 2390–2391.

54. Gillitzer, E., Suci, P., Young, M., and Douglas, T. (2006). Controlled ligand display on a symmetrical protein-cage architecture through mixed assembly. Small *2*, 962–966.

55. De Schrijver, M. (1989). Scintigraphy of Inflammation with Nanometer-Sized Colloidal Tracers (London: Kluwer Academic Publishers).

56. Moghimi, S.M., Hunter, A.C., and Murray, J.C. (2001). Long-circulating and target-specific nanoparticles: theory to practice. Pharmacol. Rev. *53*, 283–318.

57. Robinson, A.M., Creeth, J.E., and Jones, M.N. (2000). The use of immunoliposomes for specific delivery of antimicrobial agents to oral bacteria immobilized on polystyrene. J. Biomater. Sci. Polym. Ed. *11*, 1381–1393.

58. Wimpenny, J., Manz, W., and Szewzyk, U. (2000). Heterogeneity in biofilms. FEMS Microbiol. Rev. *24*, 661–671.

59. Ahmed, K., Gribbon, P., and Jones, M.N. (2002). The application of confocal microscopy to the study of liposome adsorption onto bacterial biofilms. J. Liposome Res. *12*, 285–300.

60. Marraffini, L.A., DeDent, A.C., and Schneewind, O. (2006). Sortases and the art of anchoring proteins to the envelopes of gram-positive bacteria. Microbiol. Mol. Biol. Rev. *70*, 192–221.

61. Patel, A.H., Nowlan, P., Weavers, E.D., and Foster, T. (1987). Virulence of protein-a-deficient and α-toxin-deficient mutants of *Staphylococcus aureus* isolated by allele replacement. Infect. Immun. *55*, 3103–3110.

62. Wu, A.M., and Senter, P.D. (2005). Arming antibodies: prospects and challenges for immunoconjugates. Nat. Biotechnol. *23*, 1137–1146.

63. Bernardo, K., Fleer, S., Pakulat, N., Krut, O., Hunger, F., and Kronke, M. (2002). Identification of *Staphylococcus aureus* exotoxins by combined sodium dodecyl sulfate gel electrophoresis and matrix-assisted laser desorption/ionization-time of flight mass spectrometry. Proteomics *2*, 740–746.

64. Harrison, J.J., Ceri, H., Stremick, C., and Turner, R.J. (2004). Differences in biofilm and planktonic cell mediated reduction of metalloid oxyanions. FEMS Microbiol. Lett. *235*, 357–362.

65. Zimmerli, W., Frei, R., Widmer, A.F., and Rajacic, Z. (1994). Microbiological tests to predict treatment outcome in experimental device-related infections due to *Staphylococcus aureus*. J. Antimicrob. Chemother. *33*, 959–967.

66. Harris, L.G., Foster, S.J., and Richards, R.G. (2002). An introduction to *Staphylococcus aureus*, and techniques for identifying and quantifying *S. aureus* adhesins in relation to adhesion to biomaterials. Eur. Cell. Mater. *4*, 39–60.

67. Wang, Q., Lin, T.W., Johnson, J.E., and Finn, M.G. (2002). Natural supramolecular building blocks: cysteine-added mutants of cowpea mosaic virus. Chem. Biol. *9*, 813–819.

68. Chatterji, A., Ochoa, W.F., Paine, M., Ratna, B.R., Johnson, J.E., and Lin, T.W. (2004). New addresses on an addressable virus nanoblock: uniquely reactive lys residues on cowpea mosaic virus. Chem. Biol. *11*, 855–863.

69. Allen, M., Bulte, J.W.M., Liepold, L., Basu, G., Zywicke, H.A., Frank, J.A., Young, M., and Douglas, T. (2005). Paramagnetic viral nanoparticles as potential high-relaxivity magnetic resonance contrast agents. Magn. Reson. Med. *54*, 807–812.

70. Rennen, H., Boerman, O.C., Oyen, W.J.G., and Corstens, F.H.M. (2001). Imaging infection/inflammation in the new millennium. Eur. J. Nucl. Med. *28*, 241–252.

71. Morawski, A.M., Winter, P.M., Crowder, K.C., Caruthers, S.D., Fuhrhop, R.W., Scott, M.J., Robertson, J.D., Abendschein, D.R., Lanza, G.M., and Wickline, S.A. (2004). Targeted nanoparticles for quantitative imaging of sparse molecular epitopes with MRI. Magn. Reson. Med. *51*, 480–486.

72. Jaffer, F.A., and Weissleder, R. (2005). Molecular imaging in the clinical arena. JAMA *293*, 855–862.

73. Leid, J.G., Shirtliff, M.E., Costerton, J.W., and Stoodley, P. (2002). Human leukocytes adhere to, penetrate, and respond to *Staphylococcus aureus* biofilms. Infect. Immun. *70*, 6339–6345.

74. Ahrens, E.T., Rothbacher, U., Jacobs, R.E., and Fraser, S.E. (1998). A model for MRI contrast enhancement using T-1 agents. Proc. Natl. Acad. Sci. USA *95*, 8443–8448.

75. Stewart, P.S. (1998). A review of experimental measurements of effective diffusive permeabilities and effective diffusion coefficients in biofilms. Biotechnol. Bioeng. *59*, 261–272.

76. Debeer, D., Stoodley, P., Roe, F., and Lewandowski, Z. (1994). Effects of biofilm structures on oxygen distribution and mass-transport. Biotechnol. Bioeng. *43*, 1131–1138.

77. Marrie, T.J., Nelligan, J., and Costerton, J.W. (1982). A scanning and transmission electron-microscopic study of an infected endocardial pacemaker lead. Circulation *66*, 1339–1341.

78. Nickel, J.C., Gristina, A.G., and Costerton, J.W. (1985). Electron-microscopic study of an infected Foley catheter. Can. J. Surg. *28*, 50–51, 54.

79. Kadurugamuwa, J.L., Sin, L., Albert, E., Yu, J., Francis, K., DeBoer, M., Rubin, M., Bellinger-Kawahara, C., Parr, T.R., and Contag, P.R. (2003). Direct continuous method for monitoring biofilm infection in a mouse model. Infect. Immun. *71*, 882–890.

80. Fluckiger, U., Ulrich, M., Steinhuber, A., Doring, G., Mack, D., Landmann, R., Goerke, C., and Wolz, C. (2005). Biofilm formation, icaADBC transcription, and polysaccharide intercellular adhesin synthesis by Staphylococci in a device-related infection model. Infect. Immun. *73*, 1811–1819.

81. Monzon, M., Garcia-Alvarez, F., Lacleriga, A., Gracia, E., Leiva, J., Oteiza, C., and Amorena, B. (2001). A simple infection model using pre-colonized implants to reproduce rat chronic *Staphylococcus aureus* osteomyelitis and study antibiotic treatment. J. Orthop. Res. *19*, 820–826.

82. Drummond, D.C., Meyer, O., Hong, K.L., Kirpotin, D.B., and Papahadjopoulos, D. (1999). Optimizing liposomes for delivery of chemotherapeutic agents to solid tumors. Pharmacol. Rev. *51*, 691–743.

83. Harisinghani, M.G., Saksena, M., Ross, R.W., Tabatabaei, S., Dahl, D., McDougal, S., and Weissleder, R. (2005). A pilot study of lymphotrophic nanoparticle-enhanced magnetic resonance imaging technique in early stage testicular cancer: a new method for noninvasive lymph node evaluation. Urology *66*, 1066–1071.

84. Kaiser, C.R., Flenniken, M.L., Gillitzer, E., Harmsen, A.G., Harmsen, A.L., Jutila, M.A., Douglas, T., and Young, M. (2006). Biodistribution studies of protein cage nanoparticles demonstrate broad tissue distribution and rapid clearance in vivo. Int. J. Nanomed.

85. Shen, T., Weissleder, R., Papisov, M., Bogdanov, A., and Brady, T.J. (1993). Monocrystalline iron-oxide nanocompounds (MION): physicochemical properties. Magn. Reson. Med. *29*, 599–604.

86. Raja, K.S., Wang, Q., Gonzalez, M.J., Manchester, M., Johnson, J.E., and Finn, M.G. (2003). Hybrid virus-polymer materials. 1. Synthesis and properties of PEG-decorated cowpea mosaic virus. Biomacromolecules *4*, 472–476.

87. Bancroft, J.B., and Hiebert, E. (1967). Formation of an infectious nucleoprotein from protein and nucleic acid isolated from a small spherical virus. Virology *32*, 354–356.

88. Basu, G., Allen, M., Willits, D., Young, M., and Douglas, T. (2003). Metal binding to cowpea chlorotic mottle virus using terbium(III) fluorescence. J. Biol. Inorg. Chem. *8*, 721–725.

89. Speir, J.A., Bothner, B., Qu, C.X., Willits, D.A., Young, M.J., and Johnson, J.E. (2006). Enhanced local symmetry interactions globally stabilize a mutant virus capsid that maintains infectivity and capsid dynamics. J. Virol. *80*, 3582–3591.

90. Wann, E.R., Fehringer, A.P., Ezepchuk, Y.V., Schlievert, P.M., Bina, P., Reiser, R.F., Hook, M.M., and Leung, D.Y.M. (1999). *Staphylococcus aureus* isolates from patients with Kawasaki disease express high levels of protein A. Infect. Immun. *67*, 4737–4743.

91. Yarwood, J.M., McCormick, J.K., and Schlievert, P.M. (2001). Identification of a novel two-component regulatory system that acts in global regulation of virulence factors of *Staphylococcus aureus*. J. Bacteriol. *183*, 1113–1123.

92. Spurr, A.R. (1969). A low-viscosity epoxy resin embedding medium for electron microscopy. J. Ultrastruct. Res. *26*, 31–43.

93. Reynolds, E.S. (1963). The use of lead citrate at high pH as an electron-opaque stain in electron microscopy. J. Cell Biol. *17*, 208–212.

